Carbon 203 (2023) 436–444

Contents lists available at ScienceDirect

Carbon

journal homepage: www.elsevier.com/locate/carbon

Nanofiber-in-microfiber carbon/silicon composite anode with high silicon content for lithium-ion batteries

Yixian Pei [a], Yuxin Wang [b], An-Yi Chang [b], Yixin Liao [b], Shuan Zhang [a], Xiufang Wen [a,*], Shengnian Wang [b,**]

[a] School of Chemistry and Chemical Engineering, South China University of Technology, Guangzhou, Guangdong, 510640, China
[b] Chemical Engineering, Institute for Micromanufacturing, Louisiana Tech University, PO Box 10137, Ruston, LA, 71272, USA

ARTICLE INFO

Keywords:
Silicon-rich anode
Nanofiber
Microfiber
Lithium-ion batteries
Composites

ABSTRACT

Silicon-rich anodes are desired to leverage the energy capacity of lithium-ion batteries (LIBs) towards critical markets. We prepared new silicon-rich composite anodes with a nanofiber-in-microfiber architecture using a co-axial electrospinning setup. A polyvinyl alcohol (PVA) solution that allows high silicon content serves as the central stream, which holds silicon nanoparticles into short, branched composite nanofibers. These nanofibers were wrapped by long, ductile microfibers made of polyacrylonitrile (PAN) that is supplied in the sheath fluid. After carbonization, the received carbon/silicon composites were tested as the anode of LIBs, in which the silicon-rich nanofibers host the majority of lithium ions while their thin carbon skin originated from PVA promotes the conductivity and charge transfer. The outside PAN-derived microfibers provide needed structural support for those encapsulated silicon-rich nanofibers, making the final composites also an integrated, three-dimensional current collector. The nanofibrous morphology and the void space in between help accommodate the notorious volume expansion issues during lithiation/delithiation. The new composites were confirmed on their nanofiber-in-microfiber configuration. With a Si content of 40%, this unique fibrous anode material achieves ~900 mAh g^{-1} specific capacity and ~90% capacity retention from cycle 50 to cycle 250 by effectively balancing some major challenges associated with silicon-rich anodes.

1. Introduction

Rechargeable lithium-ion batteries (LIBs) dominate current mobile electronics market because of their high energy density, long cycle life, and promising power performance [1–3]. However, commercial LIBs have been stretched to nearly their capacity limit with current metal oxide cathodes and graphite anodes while not yet meet the need on energy density (energy/volume) and specific capacity (energy/weight) from other critical energy storage applications such as electric transportation or stationary power storage that need much large energy/-power capacity [4,5]. Tremendous efforts have been made in the past decade on the search for new active materials and/or desired configurations of electrodes for LIBs [6–9]. The adoption of silicon/carbon composites seems a natural solution of challenges on the anode materials for their potential heritage of merits from carbon (high electrical conductivity) [10,11] and silicon (high lithium capacity) [12–14]. Among various silicon/carbon composite anode materials, nanostructured silicon, including nanoparticles [15–17] and nanowires [18–20], are preferred silicon formats to mitigate the adverse challenges in silicon anodes, namely the electrode pulverization and capacity loss during repeated charge/discharge cycles due to dramatic volume change (more than 300%) and consequent stress induction [21]. Despite their success on improving capacity retention and cycling stability, the adoption of nanostructured silicon still faces many challenges in compliance with existing manufacturing lines. The synthesis of silicon nanowires generally involves wet-chemical processes, toxic silane gas, and/or templates [22–24], which are often too expensive and undesired during scaling up. Although silicon nanoparticles are available in large-scale, dispersing them in carbon matrix via simply mechanical mixing or ball milling processes did not work well in the aspect of improving cycling stability and capacity retention, particularly for anodes of large energy density that demand high silicon content [25–27].

* Corresponding author.
** Corresponding author.
E-mail addresses: xfwen@scut.edu.cn (X. Wen), swang@latech.edu (S. Wang).

https://doi.org/10.1016/j.carbon.2022.11.100
Received 12 July 2022; Received in revised form 7 November 2022; Accepted 30 November 2022
Available online 2 December 2022

Composites with "core-shell", "shell-core-shell", or "yolk-shell" structure with silicon nanoparticles or nanowires in carbon nanofibers were found working better [28–33]. Their one-dimensional nanostructure network allows quick transport of lithium ions to active elements (e.g., silicon) and high lithiation/delithiation efficiency [32]. Moreover, the continuous, interconnected network structure gives them privilege as the current collector when used as anode and no need for additional binding materials [33,34].

Despite their successful proof-of-concept, the silicon/carbon composite anodes still face great challenges on their processing and manufacturing for high throughput and desired performance [35–38]. High solid content is essential for silicon-based anode materials of large energy capacity while their continuous addition in polymer contributes to a dramatic increase of the viscosity of the processing fluid after passing a critical solid percentage. Beyond the maximum silicon mass allowance in a particular polymer solution, the fiber production becomes very challenging, which lead to collapsed nanofibers or nanofibers that lose ductility. For example, as the most popular carbon nanofiber material, polyacrylonitrile (PAN), it allows up to 40% of mass content of silicon in its N, N-dimethylformamide (DMF) solution with reasonable processing pressure drop during fluid transport [39]. In contrast, a poly (vinyl alcohol) aqueous solution allows up to 80% silicon, but still has acceptable processing viscosity [40]. However, high carbon loss of PVA during further carbonization makes the carbon/-silicon nanofibers derived from PVA/Si composites easily lose flexibility or even pulverization of their nanofiber structure. Therefore, if their silicon content becomes very high, binding materials must be added to stitch the broken short composite nanofibers together. To achieve composite nanofibers with high silicon content and ductility of long fiber network, we present here a nanofiber-in-microfiber composite configuration with rich silicon content and ductile fiber mat morphology. The new silicon/carbon composites were prepared through a coaxial electrospinning process (Fig. 1a). A PVA aqueous solution was used as the middle electrospinning fluid in which silicon nanoparticles (25–50% content) were dispersed prior to electrospinning. A PAN/DMF (5–10 wt%) solution was introduced in the sheath stream to wrap up the silicon-rich nanofibers, serving as ductile shell to help hold the fibrous structure of inside silicon-rich composites after the great mass loss of PVA during later carbonization in N_2 gas. In these fibrous silicon/carbon composites (Fig. 1b), silicon serves as the active materials for Li ion host; PVA helps hold silicon nanoparticles in a short nanofiber format; PAN works as the outer support layer to retain the fibrous morphology to provide the essential electron conductivity and flexibility needed as collector-free anodes. The produced nanofiber-in-microfiber carbon/-silicon composite were further assembled into batteries and tested for their electrochemical performance.

2. Experimental

2.1. Chemicals

Polyacrylonitrile (PAN, average MW 150,000), N, N-dimethylformamide (DMF, 99.8%), Polyvinyl alcohol (PVA, average MW 75,000), lithium hexafluorophosphate ($LiPF_6$, 99.99%), ethylene carbonate (EC, 99%), and diethyl carbonate (DEC, 99%), were purchased from Sigma-Aldrich (St Louis, MO). Silicon nanoparticles with an average diameter of ~20 nm were purchased from MTI Corporation (Richmond, CA). All chemicals were used without further purification unless specified.

2.2. Materials preparation

The nanofiber-in-microfiber composite mat was prepared using a coaxial electrospinning process, followed by carbonization. Typically, PAN/DMF (2–5 wt%) and PVA/H_2O (10 wt%) solutions were first prepared. Silicon nanoparticles (25–50 wt%) were then dispersed in the pre-made PVA aqueous solution under agitation. The PVA/Si suspension was then loaded as the inner fluid of the co-axial electrospinning setup (see Fig. 1a) and pumped at a flow rate of 0.75 ml h^{-1} through the center metallic nozzle. A PAN/DMF solution was loaded as the sheath fluid. A directional current electric bias (24 kV) was added between the central metallic needle end and a grounded aluminum pan collector with a needle-to-collector distance of 15 cm through Gamma ES-40P power supply (Gamma High Voltage Research, Inc). The electrospun composite fibers (denoted as "PVA/Si/PAN") were then collected and stabilized in air at 280 °C for 6 h (with a heating rate of 5 °C min^{-1}). The fiber mats were further carbonized at 700 °C for 1 h in argon gas (with a heating rate of 2 °C min^{-1}, following a common protocol as in Ref. [39]) to produce nanofiber-in-microfiber carbon/silicon composite nanofibers (denoted as "C/Si composite fibers" in later description). For comparison purpose, PVA/Si composite nanofibers (without the addition of PAN coating) were also prepared and carbonized in the same process (denoted as "PVA/Si").

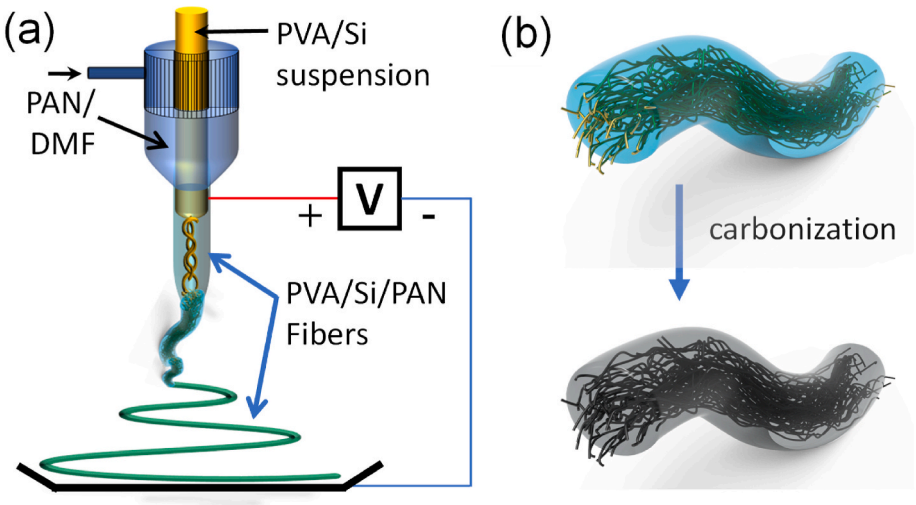

Fig. 1. Schematic of the coaxial electrospinning process in the manufacture of nanofiber-in-microfiber composite fiber mat (a) and the 3D anode configuration with Si/PVA nanofiber bundles in PAN microfiber before and after carbonization (b). (A colour version of this figure can be viewed online.)

2.3. Characterization

Scanning electron microscopy (SEM) images were taken using a Hitachi S-4800 instrument at 1.0 or 3.0 kV as specified in figures. All samples were sputter coated with gold to reduce the potential charging effect except for those that were used for the energy-dispersive X-ray spectroscopy (EDS) measurement. The energy-dispersive X-ray spectroscopy (EDS) was conducted at 10 kV by a Bruker EDS XFlash 6160 module installed on the SEM instrument. Element mapping was done using ESPRIT software to generate the distribution images of each element and calculate their percentages in the composite samples. The cross-section structure of composite fibers was characterized by transmission electron microscopy (TEM, JEOL 1400, JEOL).

Thermo-gravimetric analysis (TGA) was done to monitor the weight loss of nanofiber samples using a TGA 2050 Thermogravimetric Analyzer (TA Instruments, Inc). The thermal scanning was performed from 30 to 800 °C at a ramp rate of 10 °C min^{-1} in air environment.

The X-ray photoelectron spectroscopy (XPS) analysis was done on a Scienta Omicron instrument with the following operation conditions: 10 sweeps for the survey scans and 200 sweeps for each of C 1s, Si 2p and N 1s detailed scan. The pass energy was set to 40 eV with a step size of 0.2 eV and the dwell time of 200 ms for all samples.

X-ray diffraction (XRD) patterns were recorded on a Bruker D8 Advance X-ray diffractometer using Cu Kα radiation at room temperature at 40 kV and 40 mA. Data was collected with the 2θ range of 6–90° at a step size of 0.02°.

2.4. Electrochemical evaluation

Electrochemical performance was evaluated using the standard 2032 coin cells (MTI Corp). The produced nanofiber mats (~3 mg) were directly used as the working electrode without adding any binder or conductive materials. Lithium chips of 250 μm in thickness (MTI Corp) and polypropylene membrane (Celgard, LLC) of 25 μm in thickness were used as the counter electrode and separator, respectively. The electrolyte solution used in tests was 1 M $LiPF_6$ in 1:1 (v/v) EC: DEC. Coin cells were assembled in a high-purity argon-filled glove box. The galvanostatic charge/discharge characteristics were recorded with an MTI battery-testing system (model number BST8-WA) in a voltage range of 0.01–2.0 V with a current density of 50 mAg^{-1} at room temperature. Electrochemical impedance spectroscopy (EIS) measurements were conducted on CHI 760E electrochemical workstation. The ac perturbation signal was set at 5 mV with a frequency range of 10^{-1} -10^{5} Hz. The Zview2 software was used to extract the parameters of electronic units in a pre-set equivalent electronic circuit of the tested batteries.

3. Results and discussions

The morphology of the PVA/Si/PAN composites fibers are shown in Fig. 2. As the PAN outer layer is thick enough to fully wrap up the inside PVA/Si nanofibers, the composite microfibers have taut and smooth surface (Fig. 2a & supp Figure 1a). The average diameter of these composite microfibers varies from 5 to 9 μm, on which silicon nanoparticles or polymer nanofibers scatteredly attached. Inside microfibers, porous structures made of PVA/Si nanofibers can be clearly seen (Fig. 2b & supp Figure 1b). To reveal how PVA/silicon nanofibers are wrapped inside PAN microfibers, TEM images of the composite microfibers were taken. As shown in Fig. 2c & supp Figure 1b, PVA/Si nanofibers with an average diameter 300–600 nm present with well-reserved nanofiber morphology. Silicon nanoparticles are encapsulated in individual PVA nanofibers like bead chains (Fig. 2c). Occasional aggregations are found inside nanofibers at entangled locations (inset of Fig. 2c). Element mapping was done using EDS to further reveal the dispersion status of silicon nanoparticles in composite microfibers. As shown in Fig. 2d, silicon nanoparticles distribute uniformly in the carbon domains of the composite microfibers.

As carbonization leaves only thin carbon skin on PVA/Si nanofibers to maintain their integrity, the carbonized composites are further used to discover the overall assembly status of silicon nanoparticle in original composite fibers. PVA/Si nanofibers with different initial silicon-to-polymer mixing ratios were made by replacing the sheath fluid with solvent only in the co-electrospinning setup. Comparison was made on both the large and microscale morphology of the composite nanofibers before and after carbonization. As shown in Fig. 3a, when the silicon content is low (e.g., Si/PVA = 1:3 or 25 wt%), the composite nanofibers show typical smooth surface of the electrospun nanofibers. After

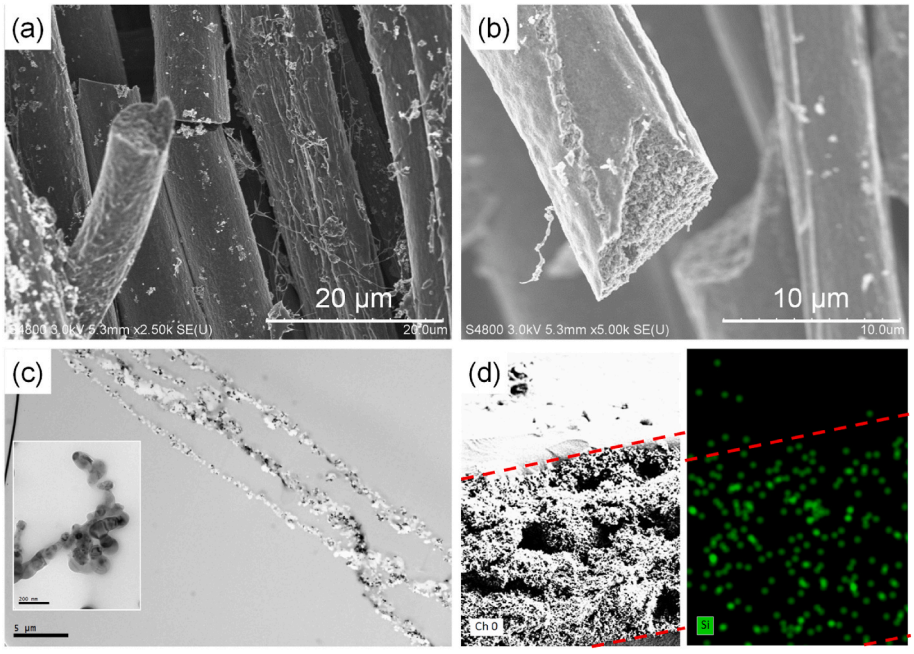

Fig. 2. Images of SEM (a, b), TEM (c), and EDS elemental mapping (d) of PVA/Si/PAN fibers with an original Si/PVA ratio of 1:3 (or 25 wt%). Panel d has the boundary of a microfiber outlined in dashed red line. (A colour version of this figure can be viewed online.)

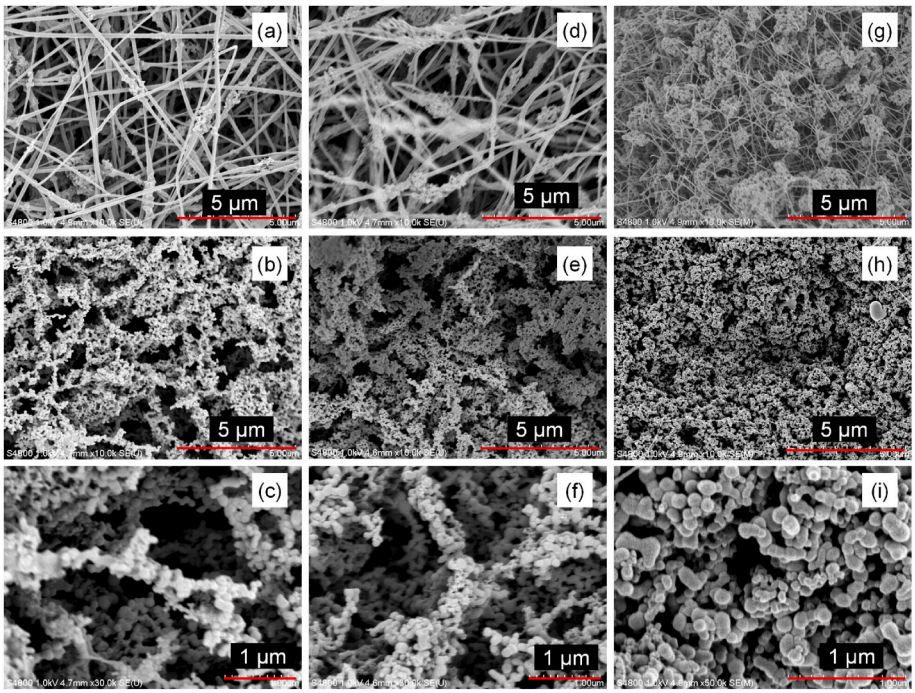

Fig. 3. SEM images of PVA/Si composite nanofibers with a Si/PVA ratio of (a) 1:3; (d) 2:3; (g) 3:3 and their carbonized counterparts in low magnification (b, e, h) and high magnification (c, f, i), respectively. (A colour version of this figure can be viewed online.)

carbonization, Si nanoparticles are found assembled as short (sub-micrometer) nanofibers with their fibrous branches held together by the carbon skin derived from PVA (Fig. 3b & c). The produced carbon/silicon composite nanofiber mats are very flexible because of the relatively thick carbon layer and strong linkages left in the nanofiber network. When more silicon nanoparticles added (e.g., Si/PVA = 2:3 or 40 wt% in the electrospinning solution), aggregates start appearing randomly in some locations of the electrospun nanofibers, resulting in rough and uneven surface, though most silicon nanoparticles are still encapsulated in composite nanofibers (Fig. 3d). Silicon domains get larger in some locations and their fibrous morphology therefore becomes less obvious (Fig. 3e & f). The diameter of those short silicon fibers slightly increases due to denser nanoparticle aggregates and possible dislocations of neighbor silicon domains during PVA calcination. Such aggregation becomes more serious when the initial silicon/PVA mixing ratio was increased to 1:1 (or 50 wt%). Many cage-like islands of 1–2 μm in size, with silicon nanoparticles stitched together by composite nanofibers, emerge in the composite nanofiber network (Fig. 3g). More dense silicon domains appear with less fiber-like morphology (Fig. 3h & i). The free space between silicon branches largely shrunk, though very thin nanofibers can still be seen in some locations, connecting different silicon-rich domains. Similar Si morphology was confirmed with a SEM image on some broken area of the fibrous composites with PAN-derived carbon shell (supp Figure 1 c).

During carbonization, a large percentage of carbon in PVA/Si nanofibers lost, which helps leverage the silicon/carbon ratio in the final C/Si composites. EDS analysis (Fig. 4a &4b) shows that for a sample of PVA/Si composite nanofibers with an original carbon/silicon ratio of 2:1 before carbonization (C: 62 wt%; Si: 32 wt%), the ratio changes to 3.3:1 after carbonization (C: 22 wt%; Si: 72 wt%). Although carbonization raises the eventual silicon percentage, it costs the ductility of those nanofibers on many occasions. Unlike the composite nanofibers with a silicon content of 25 wt% or 40 wt%, the one with 50 wt% silicon, though their shape and morphology were reserved on substrate after carbonization, great care must be taken when handling those composite fiber mats to avoid pulverization. This disqualifies their use as flexible 3D current collector and makes them not much different from those

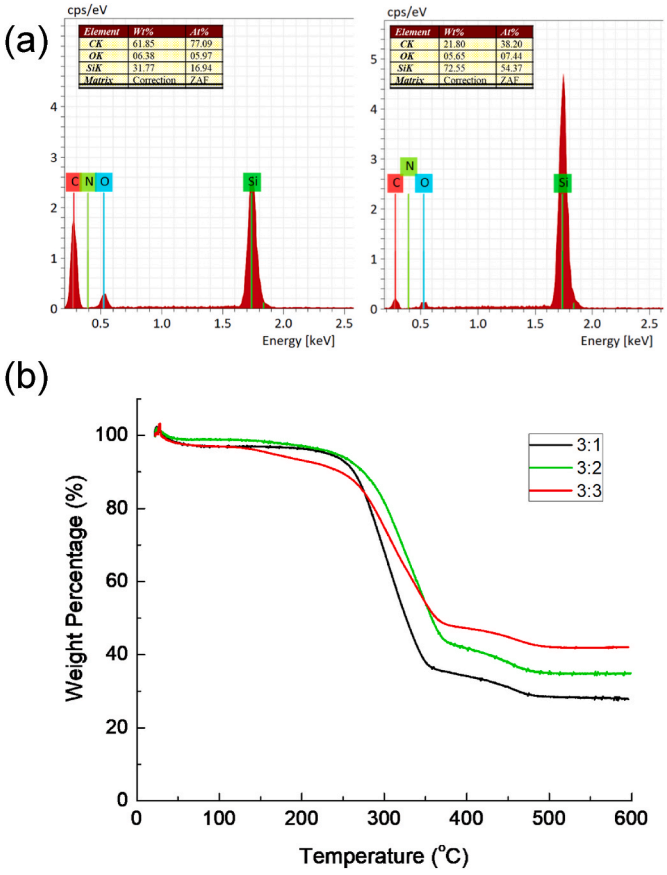

Fig. 4. EDS quantitative analysis (a) of PVA/Si/PAN fibers before and after carbonization with an original Si/PVA ratio of 1:3. (b) TGA analysis of C/Si fibers with various carbon/Si ratios. (A colour version of this figure can be viewed online.)

composite anodes that were made by physically mixing conductive carbon and silicon nanoparticles. After introducing a layer of PAN to wrap up the PVA/Si nanofiber bundles, the produced silicon-rich composite microfibers become ductile again after carbonization. With nearly 40–60% of the original carbon molecules is retained after cyclization of carbon atoms, this PAN-derived fibrous shell provides mechanical strength to the composite microfiber mat while protect the thin silicon/carbon nanofibers insides to hold their morphology to avoid pulverization. The actual Si/C ratio of the carbonized PVA/Si/PAN composite fibers was measured by TGA. As shown in Fig. 4b, the TGA curves for all composite fibers have a clear weight loss stage between 250 and 450 °C, contributed by the burn out of carbon content. The weight loss percentage matches closely enough to the polymer content in the original PVA/Si nanofibers. The PAN microfiber shell that encapsulates PVA/Si nanofiber bundles compensates the lost carbon from PVA carbonization in the final carbon/silicon composites. It not only provides the flexibility and high silicon content of the composite fibers needed as anode material of LiBs, but also the processing allowance of the original polymer/silicon suspensions.

The XRD data of the carbonized PVA/Si/PAN composite fibers is given in supp Figure 2a. It clearly exhibits the diffraction peaks (2θ = 28.4°, 47.3°, 56.1°, 69.3°, 76.5°, and 88.1°) of the (111), (201), (311), (400), and (331) crystal planes of Si in its face-centered cubic structure. This confirms that the dominant crystalline Si inside the C/Si composites after carbonization. A broad peak at the 2θ of 20°–30°, instead of a sharp peak of the (002) plane of graphite at 26.7° is presented, which is typical for carbon fibers. To verify the graphitization degree of carbon in the C/Si fibrous composites, Raman spectrum was collected (supp Figure 2b). The typical D band at 1348 cm^{-1} and G band at 1563 cm^{-1} show up, corresponding to the disordered structure and the graphitic carbon domain respectively. After analyzing the peak area of these two overlapped bands, an intensity ratio (I_D/I_G) was found close to 1.2, indicating the existing of the graphene structure, while not fully organized graphite carbon on the surface of the composite fibers. Carbon atoms in this nanofiber-in-microfiber C/Si composite samples stays as a mixture of amorphous and crystallized states.

The XPS spectrum of the carbonized PVA/Si/PAN fibers shows clearly the N 1s peak besides the major peaks of carbon, oxygen, and silicon elements when compared to the survey spectrum of the PVA/Si nanofiber sample (Fig. 5a). A contribution of ~4.4% of the total mass in the composites proves the presence of nitrogen. Further deconvolution of the N 1s spectrum in a high-resolution scan reveals the existing pyridinic (398.4 eV) and pyrrolic (400.4 eV) groups, confirming the various formats of cyclization of PAN molecules in the C/Si composites (Fig. 5b). The Si 2p spectrum displays two main peaks centered at 99.6 eV (Si $2P_{3/2}$), 100.3 eV (Si $2P_{1/2}$), and 103.6 eV, corresponding to Si (Si^0) and SiO_2 (Si^{4+}) phase, respectively, as shown in Fig. 5c & d. The area ratio of these two spin orbit peaks (Si $2P_{3/2}$/Si $2P_{1/2}$) is close to 3/2. Other subpeaks in between are attributable to some non-stoichiometric SiOx bonds (including Si^{1+} at 100.8 eV, Si^{2+} at 101.5 eV, Si^{3+} at 102.4 eV) [41]. A large percentage of SiO_2 (Si^{4+}) phase (~65%) was found on the surface Si nanoparticles of the PVA/Si composite nanofibers (Fig. 5d), while in PVA/Si/PAN composite fibers, this percentage drops to ~ 50% (Fig. 5c). Two major processes probably contribute to the SiO_2 shell: one is the native passive layer on the surface of Si nanoparticles, which is unavoidable given their initial presence in an aqueous PVA solution. Although HF pre-etching before mixing with the PVA solution can help strip this native oxide layer, Si nanoparticles would be quickly re-oxidized due to their long residence time in the PVA solution during the nanofiber processing step. The followed drying and stabilization of the formed composite nanofibers at elevated temperature may further contribute to additional oxidization by moisture, which, however, is necessary before polymer carbonization to help form high-quality carbon fibers. Compared to PVA/Si nanofibers, the extra PAN coating seems helpful to mitigate this second oxidation process during fiber stabilization, leaving less oxidized Si nanoparticles in the composite fibers. With lower lithiation capacity of SiO_2 phase than Si, the PVA/Si/PAN composite anode with less oxidized Si nanoparticles provides more capacity in LIBs than the PVA/Si counterpart (see next charge/discharge section for detailed discussions).

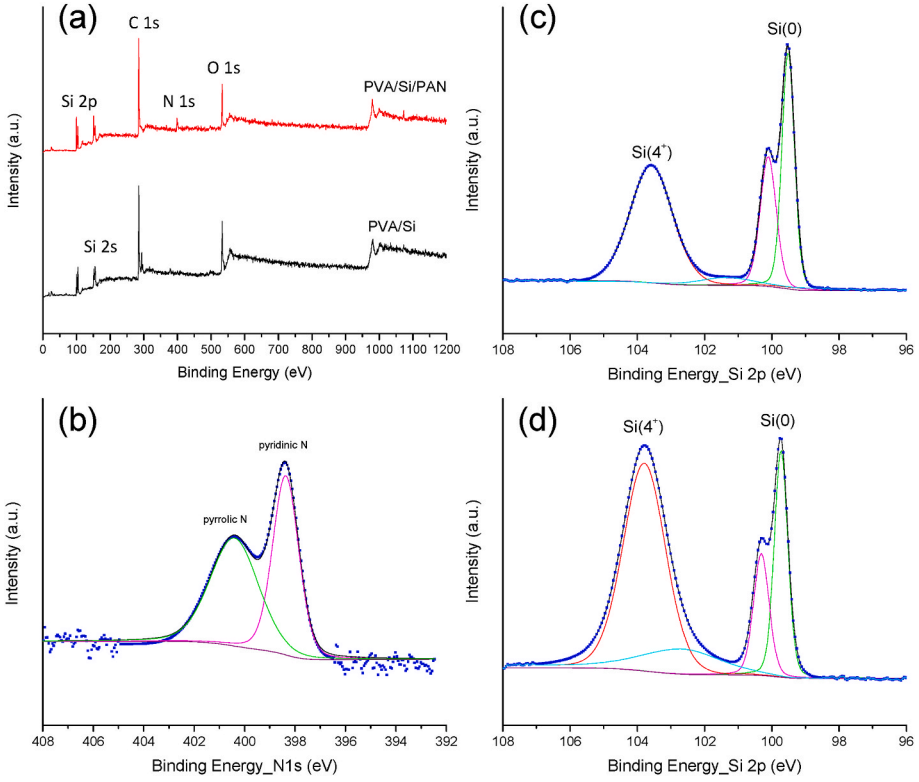

Fig. 5. XPS analysis of C/Si composite nanofibers: (a) survey scans of PVA/Si/PAN and PVA/Si composite fibers; (b–d) detailed scans of N 1s (b) and Si 2p (c) of PVA/Si/PAN fibers. Si 2p spectrum of PVA/Si nanofibers (d) is provided for comparison purpose. In panels (b–d), blue dots are the raw XPS data, black lines are the fitted curves of the whole spectrum, and curves of other colors represent either the assigned baseline or specified peaks. (A colour version of this figure can be viewed online.)

The electrochemical performance of these nanofiber-in-microfiber composite anodes was done via galvanostatic charge/discharge experiments. Fig. 6 shows the voltage profiles (plot of potential against specific capacity) at the end of 1st, 2nd, 10th, 50th, and 100th galvanostatic charge/discharge cycles of carbon/silicon composite nanofibers with initial silicon/carbon ratios from 1:3 (25 wt%) to 1:1 (50 wt%). For the first cycle, the charge and discharge capacity of the PVA/Si/PAN composite fibers with 50 wt% Si reaches 3406 mAh g^{-1} and 2401 mAh g^{-1}, respectively. As comparison, composite fiber anodes with 40 wt% Si show 2458 mAh g^{-1} (charge) and 1749 mAh g^{-1} (discharge), and the one with 25 wt% Si has the lowest capacity, only 2048 mAh g^{-1} (charge) and 1463 mAh g^{-1} (discharge). Here the capacity is calculated based on the total mass of the anode material (i.e., including both carbon and Si). It is not surprise that the composite fibrous anodes with higher Si content have larger initial storage capacity of Li ions. In the first cycle, the discharge capacity of these Si-rich composites anodes is close to the theoretical value while their charge capacity is even higher. Such phenomena are commonly seen during the initial battery tests which are believed the result of consumption of Li ions during the SEI formation [6]. The small plateau around 0.75 V on the first charging curve of all three anodes confirms the decomposition of the electrolyte solution and the formation of solid electrolyte interphase (SEI) over the electrode surface for the first time. For the same reason, low coulombic efficiency is found for all three anode types in the first cycle (and a few following cycles as well), with a coulombic efficiency (i.e., discharge capacity/charge capacity) of 70.5% (50 wt% Si anode), 71.1% (40 wt% Si anode), and 71.4% (25 wt% Si anode).

Starting from the second cycle, a second type of plateau appears on the charge and discharge curves of these Si-rich anodes at a voltage of ~0.25 V (charge) and ~0.50 V (discharge), respectively, attributed to the phase transformations between different Si–Li states during lithiation and delithiation processes [6]. After the establishment of stable SEI, the coulombic efficiency quickly recovers to nearly 100% and remained high afterwards (Fig. 6d). Like other carbon- or silicon-based anodes, gradual shrinkage of this plateau and capacity loss is also found here for all three types of Si-rich composite anodes during cycling [11]. The composites fibrous anodes with 25 wt% and 40 wt% Si show a similar plateau shrinkage and capacity decay dynamics, despite their different specific capacity values (Fig. 6a and b). For example, after 10th cycle, the discharge capacity of composite fibrous anodes lost ~12% for both composite anodes (1524 mAh g^{-1} for anodes with 40 wt% Si and 1289 mAh g^{-1} for anodes with 25 wt% Si, respectively). After 50 cycles, this value becomes 1132 mAh g^{-1} (anodes with 40 wt% Si) and 940 mAh g^{-1} (anodes with 25 wt% Si), respectively. The composite fibrous anode with 50 wt% Si has the fastest fading rate on the voltage plateau and percentage loss of the specific capacity. As shown in Fig. 6c, its discharge capacity declines to 1674 mAh g^{-1} or 70% of its initial capacity after only 10 cycles. After 50 cycles, this value drops to 1198 mAh g^{-1} or 50% of its initial capacity.

Such capacity loss dynamics is better depicted in the cycling plots of LIBs. As shown in Fig. 6d, the specific capacity loss for the anodes with 50 wt% Si shows a sharp slope than the curves from the other two anodes (with 25 wt% and 40 wt% Si). Its specific capacity value drops below that of the anodes with 40 wt% Si after 75 cycles and even below the anodes with 25 wt% Si after 125 cycles. But the other two anodes show a similar decaying rate of their specific capacities. After 10 cycles, the retention ratio of the specific capacity is 87% for the anodes with 40 wt % Si and 88% for the ones with 25 wt% Si, respectively. After 50 cycles, the retention capacity drops to 65% (for anodes with 40 wt% Si) and 64% (for anodes with 25 wt% Si) of their individual initial values. Nonetheless, the decay rate of the specific capacity for these two types of fibrous composites anodes sustains with only minor variations. This indicates that the lithiation or delithiation situations in them are similar during all testing cycles. Such similar cycling performance (except the actual capacity value) is not surprising when checking the morphology of those composite fibrous anodes: connected branch structures comprised of short Si nanofibers are seen in both composites (Fig. 3b & e), while the one with 50 wt% show many large Si islands (Fig. 3h). Ever long-term cycling stability was also examined on the fibrous composite anodes with 40 wt% Si. As shown in Fig. 6d, for over 250 cycles, their specific capacity retains ~900 mAh g^{-1} with only additional 10% loss (from cycle 50 to cycle 250). The cycling tests of triplicates were done on the composited anodes (supp Figure 3a) to confirm the reproduction of these results.

Slow decay on the specific capacity is observed for all three composite fibrous anodes during cycling rate tests (Fig. 6e). From these results, the specific charge/discharge capacity was found to catch the value received in the last cycle at the same charging current (i.e., cycle

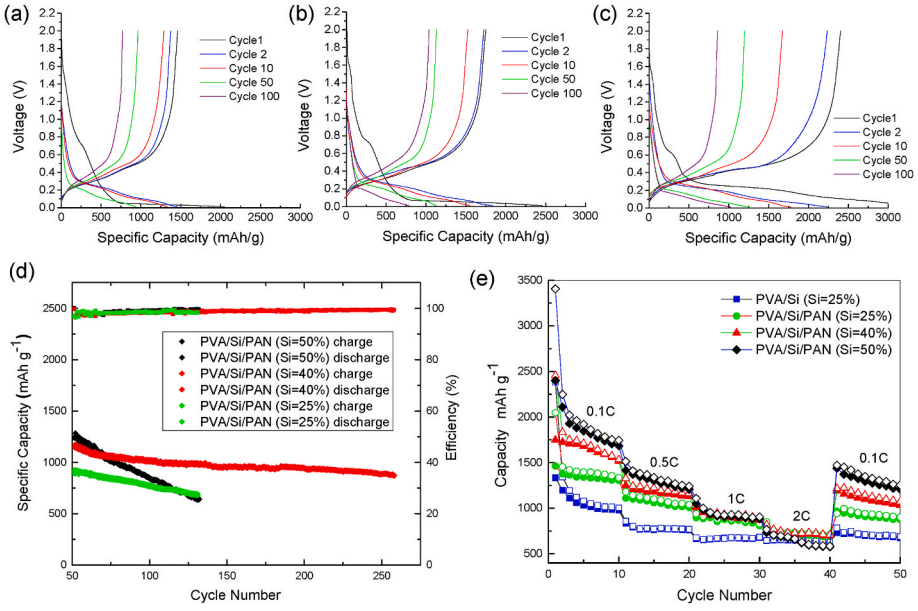

Fig. 6. (a–c) The voltage profiles for the 1st, 2nd, 10th, 50th, and 100th galvanostatic charge/discharge cycles of nanofibers-in-microfibers composite anodes with a Si ratio of 25% (a), 40% (b), and 50% (c). Different charging rates (d) and cycling performances and coulombic efficiency (e) of those PVA/Si/PAN fibers of various Si contents. (A colour version of this figure can be viewed online.)

10) like no interruption when the current rate is set back to 0.1C after a sequential increase of the current rate from 0.1C to 0.5C, 1C, and 2C. But the situation is different among anodes with different Si contents. The anodes with relatively low silicon content (i.e., 25 wt%) largely sustain the charge/discharge capacity with only minor variations. A sustained capacity of ~1000 mAh g^{-1} was found in these composite anodes (i.e., 25 wt% Si). For the composite anodes with high silicon content, the difference is more severe for the ones with 50% Si than those of 40 wt%. Nonetheless, at small current rates (0.1C and 0.5C), the charge/discharge capacity of the three anodes follows a normal order: anodes of 50% Si > anodes of 40% Si > anodes of 25% Si. But as the 50 wt% Si anodes lost quickly their capacity, this capacity ranking among the three anodes (25%, 40%, and 50% Si content) got scrambled at a current rate of 1C and 2C: the anodes with 50 wt% Si had similar or a slightly lower capacity than that with 40 wt% Si (Fig. 6e). This indicates that the key factor for stable cycling lies on the active materials with appropriate Si content and its nanoscale dimensions. Poor dispersion, obvious aggregates, or large domains of Si (e.g., anodes with 50% Si content) will result in quick capacity decay or undesired cycling performance of the electrodes.

The presence of extra carbon skin on the composite nanofiber bundles that is derived from the PAN coating indeed helps retain more lithiation capacity. Compared to the anode made of PVA/Si nanofibers alone with 25 wt% Si, the ones encapsulated in PAN microfibers settle on a higher specific capacity at various charge rates (an extra capacity of ~330 mAh g^{-1} for 0.1C, ~300 mAh g^{-1} for 0.5C, ~200 mAh g^{-1} for 1C, and ~80 mAh g^{-1} for 2C, respectively), as shown in Fig. 6e. Our previous work of nonporous C/Si nanofiber anodes with 25% Si and carbon derived from PAN received a capacity of ~570 mAh g^{-1} after 20 cycles [39]. Given the structure similarity of the nonporous C/Si nanofibers there and the ones derived from PVA in this work (~670 mAh g^{-1} at Cycle 50), their capacity is comparable considering more carbon was left from the original PAN/Si nanofibers in that reference. But when the C/Si composites anodes carry some free space around Si domains, such as the nanofiber-in-microfiber anodes in this work, a much higher reversable capacity is achieved. It seems that free space in pores or voids around Si is more important than different carbon sources, as it helps accommodate the dramatic volume change during lithiation/delithiation to delay the growth of dead silicon so that more capacity is retained during cycling than the nonporous ones.

To better understand the electrochemical performance of this nanofiber-in-microfiber C/Si composite anode, the electrochemical impedance spectra (EIS) were collected for fresh and cycled (250 cycles) batteries. Nyquist plots were made to extract information on electrolyte resistance (R_E), SEI layer resistance (R_{SEI}), and charge transfer resistance (R_{CT}). As shown in Fig. 7a, the resistance contributed by electrolyte and SEI layer is small when compared to the charge transfer resistance. A moderate increase of R_E and R_{SEI} values after cycling demonstrates the sustained conductance of the composite anode and migration of Li^+ ions to surface of the active material. A noticeable addition of R_{CT} indicates a relatively slower charge transfer kinetics after long-term cycling. The carbon shell of individual fibers that provides the needed electrically conductive network for silicon nanofibers becomes rough overall after cycling, as shown in Fig. 7b. However, the integrity of microfibers is well reserved, so does the dispersion state and morphology of silicon domains. The heterogeneity at the electrode interfaces is in consistent with the smaller "P" values of the CPE_{dl} and the Warburg element (W) in the equivalent circuit.

Full batteries with lithium manganate ($LiMn_2O_4$) cathodes to pair with our Si-rich fibrous composite anodes were assembled and tested. As shown in supp Figure 3b, stable charge/discharge behaviors are discovered, with an average capacity of ~90 mAh g^{-1} at 0.2C. The overall cycling capacity did not change significantly, which is expected as the cathode decides the total lithium supply (or storage) in full battery while anodes always have far extra host sites for lithium ions. Nevertheless, our new method enables the production of fibrous composites in competition for better silicon-rich anodes with counterparts that are made of physical mixture of conductive carbon and silicon nanoparticles. It carries high silicon content that approaches maximal processing allowance for original polymer/silicon suspensions while creates porous nanofibers for higher capacity without electrode pulverization. Besides the needed electrical conductivity, fibrous morphology reserved

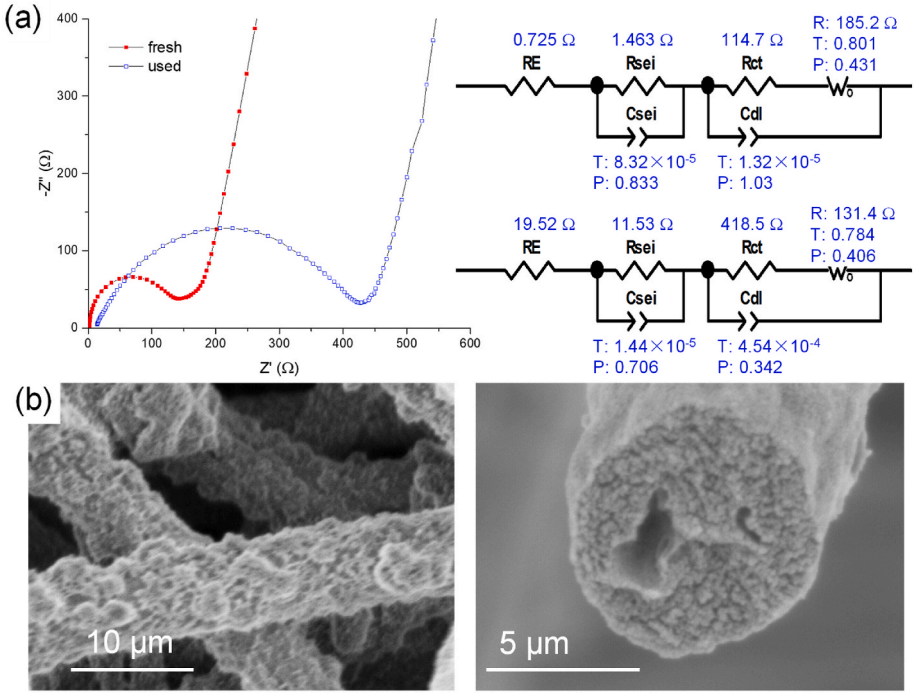

Fig. 7. (a) Nyquist plots of the EIS and the corresponding fitting on an equivalent circuit of batteries made of nanofiber-in-microfiber, Si-rich composites (40 wt%): fresh and after 250 cycles; (b) SEM images of a cycled composite fiber anode. The impedance spectrum was done with a voltage amplitude of 5 mV and a frequency range of 0.01Hz–100 kHz. (A colour version of this figure can be viewed online.)

inside the composite fiber mats to serve as flexible 3D current collector. In this unique nanofiber-in-microfiber configuration, the branched, short silicon nanofibers with thin carbon skin, together with macro-voids/mesovoids they create, appropriately manage the volume expansion and induced stress issues when lithium alloys with silicon. The outer PAN shell around PVA/silicon nanofiber bundles provides extra carbon coating to protect silicon from further oxidation during fiber processing. It also creates confined microenvironment around silicon/carbon nanofibers to limit the permeability and contact of electrolytes to silicon during cycling. This probably helps mitigate the fading of capacity, which is believed attributed to the mixed effects on the progressive increase of the SEI thickness and loss of electron conduction pathways that lead to dead silicon formation [11]. Although the situation gets improved in the C/Si composite anodes with high Si content (e.g., 40 wt%), the heterogeneous pulverization situation could not be completely avoided for anodes made of ultrahigh Si content (i.e., 50 wt % or higher) for the same reasons mentioned early about capacity fading, particularly when more micrometer size Si domains present to lose the unique configuration (i.e., short Si nanofiber bundles wrapped in long carbon microfibers), making the composite anodes similar to those blended C/Si ones. Nonetheless, both impressive Li ion storage capacity and cyclic performance are achieved when this unique composite fiber configuration is held with a silicon content of 40 wt% or less (supp table 1).

4. Conclusions

A new nanofiber-in-microfiber, Si-rich composite anode was prepared through a coaxial electrospinning, in which PVA/silicon suspension flows in the middle and a PAN/DMF solution serves as the sheath stream. The high-quality, nonwoven carbon microfibers derived from PAN outer shell provide structural protection for short, silicon-rich nanofibers inside and prevent further oxidation of silicon during fiber processing. Together with the thin carbon skin over silicon/carbon nanofiber bundles inside, the microfiber mats form an electrically conductive network to serve as the 3D current collector to promote Li ion transport and charge transfer during charge/discharge processes. Simultaneously, short silicon nanofibers and the mesoporous buffering spaces among them help effectively mitigate the induced stress in Si nanoparticles initialized by the volume change during Li insertion and extraction. All these features of this nanofiber-in-microfiber composite anode together effectively balance issues between electrode pulverization and high reversible capacity, leading to promising electrochemical performance and capacity retention for silicon-rich anodes to move forwards their commercialization. The unique processing strategy involved in this work also suggests a new route to manufacture composite nanomaterials with high solid content in broad applications beyond LIBs.

CRediT authorship contribution statement

Yixian Pei: Methodology, Investigation, Writing – original draft. **Yuxin Wang:** Methodology, Investigation. **An-Yi Chang:** Methodology, Investigation, Software. **Yixin Liao:** Investigation, Resources. **Shuan Zhang:** Visualization, Software. **Xiufang Wen:** Conceptualization, Methodology, Writing – review & editing. **Shengnian Wang:** Conceptualization, Methodology, Writing – review & editing, Supervision, Funding acquisition.

Declaration of competing interest

The authors declare the following financial interests/personal relationships which may be considered as potential competing interests: Shengnian Wang reports financial support was provided by National Science Foundation. Shengnian Wang reports financial support was provided by Louisiana Board of Regent.

Acknowledgments

We acknowledge financial support from National Science Foundation [OIA-1946231], Louisiana Board of Regent, ITRS [LEQSF (2019–20)-RD-D-07], and Louisiana Harrelson Family Professorship.

Appendix A. Supplementary data

Supplementary data to this article can be found online at https://doi.org/10.1016/j.carbon.2022.11.100.

References

[1] B. Scrosati, J. Garche, Lithium batteries: status, prospects and future, J. Power Sources 195 (2010) 2419–2430.
[2] B. Dunn, H. Kamath, J.M. Tarascon, Electrical energy storage for the grid: a battery of choices, Science 334 (2011) 928–935.
[3] M.S. Whittingham, Lithium batteries and cathode materials, Chem. Rev. 104 (2004) 4271–4301.
[4] J.M. Tarascon, M. Armand, Issues and challenges facing rechargeable lithium batteries, Nature 414 (2001) 359–367.
[5] M.M. Thackeray, C. Wolverton, E.D. Isaacs, Electrical energy storage for transportation—approaching the limits of, and going beyond, lithium-ion batteries, Energy Environ. Sci. 5 (2012) 7854–7863.
[6] C.M. Park, J.H. Kim, H. Kim, H.J. Sohn, Li-alloy based anode materials for Li secondary batteries, Chem. Soc. Rev. 39 (2010) 3115–3141.
[7] G. Jeong, Y. Kim, H. Kim, Y. Kim, H. Sohn, Prospective materials and applications for Li secondary batteries, Energy Environ. Sci. 4 (2011) 1986–2002.
[8] U. Kasavajjula, C. Wang, A.J. Appleby, Nano- and bulk-silicon-based insertion anodes for lithium-ion secondary cells, J. Power Sources 163 (2007) 1003–1039.
[9] M. Endo, C. Kim, K. Nishimura, T. Fujino, K. Miyashita, Recent development of carbon materials for Li ion batteries, Carbon 38 (2000) 183–197.
[10] L. Wang, J. Han, D. Kong, Y. Tao, Q.H. Yang, Enhanced roles of carbon architectures in high-performance lithium-ion batteries, Nano-Micro Lett. 11 (2019) 5.
[11] J. Jiang, G. Nie, P. Nie, X. Li, Z. Pan, Z. Kou, H. Dou, X. Zhang, J. Wang, Nanohollow carbon for rechargeable batteries: ongoing progresses and challenges, Nano-Micro Lett. 12 (2020) 183.
[12] X.W. Zhang, P.K. Patil, C.S. Wang, A.J. Appleby, F.E. Little, D.L. Cocke, Electrochemical performance of lithium ion battery, nano-silicon-based, disordered carbon composite anodes with different microstructures, J. Power Sources 125 (2004) 206–213.
[13] J.R. Szczech, S. Jin, Nanostructured silicon for high-capacity lithium battery anodes, Energy Environ. Sci. 4 (2011) 56–72.
[14] H. Li, X. Huang, L. Chen, Z. Wu, Y. Liang, A high capacity Nanosi composite anode material for lithium rechargeable batteries, Electrochem. Solid State Lett. 2 (1999) 547–549.
[15] R. Nava, L. Cremar, V. Agubra, J. Sánchez, M. Alcoutlabi, K. Lozano, Centrifugal spinning: an alternative for large scale production of silicon–carbon composite nanofibers for lithium ion battery anodes, ACS Appl. Mater. Interfaces 8 (2016) 29365–29372.
[16] Y. Zhang, Y. Cheng, J. Song, Y. Zhang, Q. Shi, J. Wang, F. Tian, S. Yuan, Z. Su, C. Zhou, Y. Wang, S. Yang, Functionalization-assistant ball milling towards Si/graphene anodes in high performance Li-ion batteries, Carbon 181 (2021) 300–309.
[17] H. Jia, X. Li, J. Song, et al., Hierarchical porous silicon structures with extraordinary mechanical strength as high-performance lithium-ion battery anodes, Nat. Commun. 11 (2020) 1474.
[18] C.K. Chan, H. Peng, G. Liu, K. McIlwrath, X.F. Zhang, R.A. Huggins, Y. Cui, High-performance lithium battery anodes using silicon nanowires, Nat. Nanotechnol. 3 (2008) 31–35.
[19] W.L. Xu, J.C. Flake, Composite silicon nanowire anodes for secondary lithium-ion cells, J. Electrochem. Soc. 157 (2010) A41–A45.
[20] H. Wu, Y. Cui, Designing nanostructured Si anodes for high energy lithium ion batteries, Nano Today 7 (2012) 414–429.
[21] H. Wu, G. Zheng, N. Liu, T.J. Carney, Y. Yang, Y. Cui, Engineering empty space between Si nanoparticles for lithium-ion battery anodes, Nano Lett. 12 (2012) 904–909.
[22] C.K. Chan, R.N. Patel, M.J. O'Connell, B.A. Korgel, Y. Cui, Solution-grown silicon nanowires for lithium-ion battery anodes, ACS Nano 4 (2010) 1443–1450.
[23] J. Xie, X.G. Yang, S. Zhou, D.W. Wang, Comparing one- and two-dimensional heteronanostructures as Si-based Li ion battery anode material, ACS Nano 5 (2011) 9225–9231.
[24] A. Magasinski, P. Dixon, B. Hertzberg, A. Kvit, J. Ayala, G. Yushin, High-performance lithium-ion anodes using a hierarchical bottom-up approach, Nat. Mater. 9 (2010) 353–358.
[25] Y. Li, B. Guo, L. Ji, Z. Lin, G. Xu, Y. Liang, S. Zhang, O. Toprakci, Y. Hu, M. Alcoutlabi, X. Zhang, Structure control and performance improvement of carbon nanofibers containing a dispersion of silicon nanoparticles for energy storage, Carbon 51 (2013) 185–194.

[26] L. Ji, Z. Lin, A.J. Medford, X. Zhang, Porous carbon nanofibers from electrospun polyacrylonitrile/SiO2 composites as an energy storage material, Carbon 47 (2009) 3346–3354.
[27] K. Fu, L. Xue, O. Yildiz, S. Li, H. Lee, Y. Li, G. Xu, L. Zhou, P.D. Bradford, X. Zhang, Effect of CVD carbon coatings on Si@CNF composite as anode for lithium-ion batteries, Nano Energy 2 (2013) 976–986.
[28] T.H. Hwang, Y.M. Lee, B.S. Kong, J.S. Seo, J.W. Choi, Electrospun core–shell fibers for robust silicon nanoparticle-based lithium-ion battery anodes, Nano Lett. 12 (2012) 802–807.
[29] N. Liu, H. Wu, M.T. McDowell, Y. Yao, C. Wang, Y. Cui, A yolk-shell design for stabilized and scalable Li-ion battery alloy anodes, Nano Lett. 12 (2012) 3315–3321.
[30] S.A. Klankowski, R.A. Rojeski, B.A. Cruden, J. Liu, J. Wu, J. Li, A high-performance lithium-ion battery anode based on the core-shell heterostructure of silicon-coated vertically aligned carbon nanofibers, J. Mater. Chem. 1 (2013) 1055–1064.
[31] L. Qiao, X. Sun, Z. Yang, X. Wang, Q. Wang, D. He, Network structures of fullerene-like carbon core/nano-crystalline silicon shell nanofibers as anode material for lithium-ion batteries, Carbon 54 (2013) 29–35.
[32] J. Saint, M. Morcrette, D. Larcher, L. Laffont, S. Beattie, J.P. Pérès, D. Talaga, M. Couzi, J.M. Tarascon, Towards a fundamental understanding of the improved electrochemical performance of silicon–carbon composites, Adv. Funct. Mater. 17 (2007) 1765–1774.
[33] D. Deng, J.Y. Lee, One-step synthesis of polycrystalline carbon nanofibers with periodic dome-shaped interiors and their reversible lithium-ion storage properties, Chem. Mater. 19 (2007) 4198–4204.
[34] A. Huang, Y. Ma, J. Peng, L. Li, S. Chou, S. Ramakrishna, S. Peng, Tailoring the structure of silicon-based materials for lithium-ion batteries via electrospinning technology, eScience 1 (2021) 141–162.
[35] L. Ji, A.J. Medford, X. Zhang, Fabrication of carbon fibers with nanoporous morphologies from electrospun polyacrylonitrile/poly(L-lactide) blends, J. Polym. Sci., Part B: Polym. Phys. 47 (2009) 493–503.
[36] H. Liu, C.Y. Cao, F.F. Wei, Y. Jiang, Y.B. Sun, P.P. Huang, W.G. Song, Fabrication of macroporous/mesoporous carbon nanofiber using CaCO3 nanoparticles as dual-purpose template and its application as catalyst support, J. Phys. Chem. C 117 (2013) 21426–21432.
[37] L. Ji, X. Zhang, Fabrication of porous carbon nanofibers and their application as anode materials for rechargeable lithium-ion batteries, Nanotechnology 20 (2009), 155705.
[38] C. Tran, V. Kalra, Fabrication of porous carbon nanofibers with adjustable pore sizes as electrodes for supercapacitors, J. Power Sources 235 (2013) 289–296.
[39] Y. Wang, X. Wen, J. Chen, S. Wang, Foamed mesoporous carbon/silicon composite nanofiber anode for lithium ion batteries, J. Power Sources 281 (2015) 285–292.
[40] Y.S. Kim, K.W. Kim, D. Cho, N.S. Hansen, J. Lee, Y.L. Joo, Silicon-rich carbon hybrid nanofibers from water-based spinning: the synergy between silicon and carbon for Li-ion battery anode application, Chemelectrochem 1 (2014) 220–226.
[41] H. Ma, J. Yang, J. Yang, L. Zhu, W. Huang, G. Yuan, J. Feng, T. Jen, H. Lu, Systematic study of the SiOx film with different stoichiometry by plasma-enhanced atomic layer deposition and its application I SiOx/SiO2 super-lattice, Nanomaterials 9 (2019) 55.